IEEE Access
Multidisciplinary ⋮ Rapid Review ⋮ Open Access Journal

Received 26 May 2025, accepted 10 June 2025, date of publication 19 June 2025, date of current version 11 July 2025.

Digital Object Identifier 10.1109/ACCESS.2025.3581322

RESEARCH ARTICLE

PCB-Based Dual-Polarized Liquid Crystal Reflectarray With High Aperture Efficiency and Bridge-Shaped Biasing Topology for 2D Scanning

HOGYEOM KIM[1], (Member, IEEE), BYEONGJU MOON[1], (Student Member, IEEE), SEUNGWOO BANG[1], (Graduate Student Member, IEEE), SEONGWOOG OH[2,*], (Member, IEEE), AND JUNGSUEK OH[1,*], (Senior Member, IEEE)

[1]Institute of New Media and Communication (INMC), Department of Electrical and Computer Engineering, Seoul National University, Seoul 08826, South Korea
[2]Department of Electronics Convergence Engineering, Kwangwoon University, Seoul 139-701, South Korea

Corresponding author: Jungsuek Oh (jungsuek@snu.ac.kr)

This work was supported by the Institute for Information and Communications Technology Promotion (IITP) grant funded by Korean Government (MSIT) under Grant RS 2024-00395366 by part and was supported by the Samsung Research Funding Center of Samsung Electronics under the Project Number SRFC-TE2103 by part.

*Seongwoog Oh and Jungsuek Oh contributed equally to this work.

ABSTRACT This paper presents a novel dual-linearly polarized liquid crystal reflectarray antenna (DLP-LCRA) based on a printed circuit board (PCB) process. The proposed design employs a bridge-shaped biasing topology to reduce RF losses typically associated with bias lines in PCB-based implementations. While conventional DLP-LCRAs are often fabricated using glass substrates due to the difficulty of achieving sufficiently thin bias lines in PCB processes, this work demonstrates that a cost-effective and practical solution is possible through optimized biasing structures. The proposed reflectarray cell structure and biasing scheme enable wide 2D beam scanning with high aperture efficiency. Specifically, the bridge-shaped topology mitigates polarization-dependent RF losses and supports broad beam coverage in the E-, H-, and D-planes. The influence of the biasing layer is analyzed in detail using an equivalent circuit model for TE and TM modes. Experimental results validate the performance of the proposed DLP-LCRA, achieving a maximum aperture efficiency of 46.5 %, which represents a 106.67 % improvement over state-of-the-art designs.

INDEX TERMS Dual-polarization, high aperture efficiency, liquid crystals, reflectarray, reconfigurable reflectarray, 2D beam coverage.

I. INTRODUCTION

Reflectarray antennas are planar reflector antennas comprising two-dimensional (2D) periodic patterns printed on a grounded substrate. Reflectarray antennas are extensively used in space, repeaters, and radar applications owing to their advantages, such as ease of fabrication, low weight, and low cost [1], [2], [3], [4]. Recently, several researchers have actively studied electronically controllable reflectarrays to construct scattered beams in a desired direction [5], [6], [7]. Suitable candidates for controlling the phases of the elements have been introduced, including PIN diodes, varactor diodes, and microelectromechanical system (MEMS) switches. These components were employed to change the phase responses of the cells by reversing the direction of the electric field by 180° or altering the physical dimensions.

Liquid crystals (LCs) are candidates for future midband, 5G/6G reconfigurable intelligent surface applications, such as fixed wireless access because of their low cost and broader operational band compared with other components [8], [9], [10], [11], [12], [13], [14]. In addtion, because the high frequency spectrum is a one of advantages of the LC, LC can

The associate editor coordinating the review of this manuscript and approving it for publication was Tutku Karacolak.

be candidates for antennas automotibe radar applications at the W-band [15]. Compared with the PIN and varactor diodes, the loss tangent of the LC decreases as a function of frequency. An LC-based reflectarray (LCRA) radiates scattered waves in the desired direction as the effective permittivity of the LC changes. The permittivity of an LC can be controlled by biasing the quasi-electrostatic field toward the LC cavity. When a biasing field is applied to the metallic layers, quasistatic electric fields perpendicular to the dipoles of the LC are generated, leading to a change in the LC permittivity. The main advantage of LCs is their high resolution reconfigurability, in which the permittivity can be controlled proportionally to the applied voltage. Additionally, LC technologies have already seen use in satellite communication systems and are gaining recognition as promising alternatives to mechanically reconfigurable antennas, like motorized gimbal systems.

Numerous studies have been conducted on LCRAs operating in various frequency bands [16], [17], [18], [19], [20]. In [16], a wideband LCRA in the F-band, whose electrode for the LC consisted of a multiresonant cell, was designed and demonstrated. Another wideband LCRA in the K-band was reported in [17], where a delayed biasing line of the cell provided broadband responses. In contrast to the structure in [16], the LCRA in [17] focused on the biasing line to achieve a wideband. In [18], an LCRA was introduced whose LC cell gap was modeled as a varactor diode because of the very thin cell gap. However, these reported LCRAs have limited performances, such as one-dimensional beam coverage and low aperture efficiencies [16], [18]. Moreover, although the LCRAs in [17] and [19] achieved 2D beam coverage and moderate aperture efficiency, they are only responsible for single-polarization operations because of several challenges, including the deteriorating effect of the biasing line for one polarization or imbalance of the number of biasing lines of each unit cell. The LCRA in [17] consists of a rectangular slotted metal layer, a rectangular radiating patch, and a delay line. Such a structure only operates with a single-polarized wave.

Dual-linearly polarized liquid crystal reflectarray antennas (DLP-LCRAs) have already been reported in the millimeter-wave (mmWave) band [21], [22], [23], [24]. These designs were fabricated using glass-based processes, enabling sufficiently thin bias lines to be implemented without introducing significant RF losses. Despite several advantages, glass-based processes are cost-ineffective and impose limitations on standard fabrication procedures, such as substrate stacking and via-hole drilling. Moreover, glass substrates are fragile and prone to breakage. In [21], the DLP-LCRA structure exhibited a large gain discrepancy and low sidelobe levels (SLL) due to phase errors and significant variations in reflection amplitude. Another DLP-LCRA design in [22] employed an anisotropic metal layer to control polarization. However, it faced several issues, including one-dimensional beam coverage, low aperture efficiency, and degraded SLL performance, mainly due to limited inter-layer spacing that

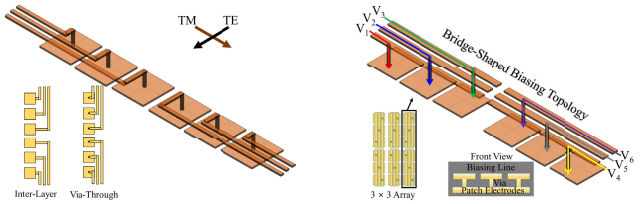

FIGURE 1. Example of the (a) conventional and (b) the proposed biasing topology.

introduced coupling effects among the metallic elements. Compared to glass-based processes, printed circuit board (PCB)-based processes are more cost-effective and widely adopted across various research fields, owing to their ease of integration with other PCB components and structural flexibility. Nevertheless, PCB-based processes pose challenges such as limited resolution in metal line width and spacing, which can cause RF losses, particularly for waves whose polarization is aligned with the metal lines. A significant advantage of the proposed DLP-LCRA, which is based on PCB processes, is that it supports mass production and can be readily extended to higher frequencies. First, the design leverages standard PCB processes, making it straightforward to implement using conventional PCB technology. Moreover, as long as the feasible resolution of PCB manufacturing is maintained, the design methodology and biasing approach proposed in this study can be applied even at higher frequencies.

This study employs PCB-based process to implement the DLP-LCRA. It is important to design the biasing layer because it affects the LCRA performance, where the biasing line is modelled as an inductance for parallel-polarized waves. In addition, the biasing layer generates an RF current, resulting in reflection loss in the LCRA. Moreover, unlike PIN diodes or varactor diodes, it is difficult to mitigate the detrimental effect of the biasing layer for single-polarization operations or to utilize a radial stub or via owing to the nature of the liquid characteristic of the LC layer.

In this study, a bridge-shaped biasing topology is introduced to enable dual-polarization responses without requiring thinning of the bias lines. Fig. 1 both the conventional and the proposed biasing topologies designed to achieve the 2D beam scanning capability. In conventional approaches, the bias lines are directly connected to the electrodes to activate the LC. There are two typical types of direct biasing topologies: inter-layer and via-through. The interlayer method places both the bias line and the electrode on the same layer, while the via-through method locates the electrode and bias line on different layers, connected through a via. To achieve dual-polarized responses, glass-based processes can suppress the RF effects of bias lines by thinning the electrodes. However, such thinning is not feasible in PCB-based processes, making it challenging to mitigate the RF losses induced by bias lines. Therefore, the impact of bias

lines must be carefully considered when implementing DLP-LCRAs. Fig. 1(b) illustrates the proposed biasing topology introduced in this study. Six different bias signals are applied along three bias lines to each patch through metallic vias. This novel biasing scheme enables dual-linearly polarized (DLP) responses, owing to the morphological uniformity of the bias lines. Furthermore, because each unit cell is excited by distinct voltage levels through the bias lines, the designed LCRA is capable of achieving 2D beam scanning.

The proposed DLP-LCRA based on the bridge-shaped biasing topology can be easily fabricated using the printed circuit board (PCB) process at a lower cost than the glass-based process. In addition, to achieve high aperture efficiency, an additional patch whose lateral dimension is larger than that of the patch electrode on the LC layer is stacked on top of the cell. The additional patch successfully suppressed the RF current caused by the bias line, resulting in a high aperture efficiency for both polarization cases. In the transverse magnetic (TM) case, an RF current is induced, causing RF losses. Finally, the proposed DLP-LCRA based on the bridged-shaped bias topology achieves maximum aperture efficiencies greater than 46.5 % and 37.8 % with SLL values of −16.5 dB and −15.3 dB for each polarization. In addition, the beam scanning ranges for the TE and TM polarizations were 0°–62° and -49°–51° and −50°–50° and 0°–60°, respectively. This study presents, for the first time, a method for designing a dual-linearly polarized liquid crystal reflectarray antenna (DLP-LCRA) using a PCB-based process in the millimeter-wave (mmWave) band, achieving wide 2D beam coverage. Moreover, the proposed design demonstrates a maximum aperture efficiency improvement of 106.67 % compared to state-of-the-art designs.

The remainder of this paper is organized as follows: Section II introduces the proposed unit cell and explains the principle of the unit cell of the LCRA and several challenges for achieving dual-polarization responses. Section III introduces the fabricated sample, and the phase extraction results for obtaining a phase-voltage graph are presented. Additionally, the measured results are discussed. Finally, Section IV concludes this paper. The equivalent circuits and corresponding real impedance simulations for the w/o and w/metallic patches are discussed in Appendix.

II. DLP-LCRA DESIGN

This section introduces the proposed bridge-shaped biasing topology for dual-polarized LCRA with 2D coverage.

Fig. 2(a) shows an enlarged view of the LCRA cell with the proposed bias topology, and Fig. 2(b) depicts the bias layer. Six bias lines were implemented because 12 × 12 cells were used in this study. A metallic via was employed to provide a bias signal to the patch electrode. The substrates utilized in this study comprised TLY-5 and FR4. The dielectric constant and loss tangent of TLY-5 were 2.2 and 0.0009, while FR4 exhibited values of 4.4 and 0.02, respectively. The relative permittivity of the LC is characterized by a complex relative permittivity (ε' - jε'') because of its loss feature. A GT7

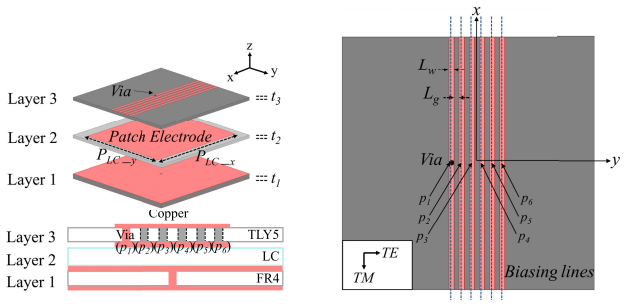

FIGURE 2. (a) Exploded view of the bridge-shaped bias topology embedded liquid crystal reflectarray (LCRA) cell and (b) the top view of the bias layer.

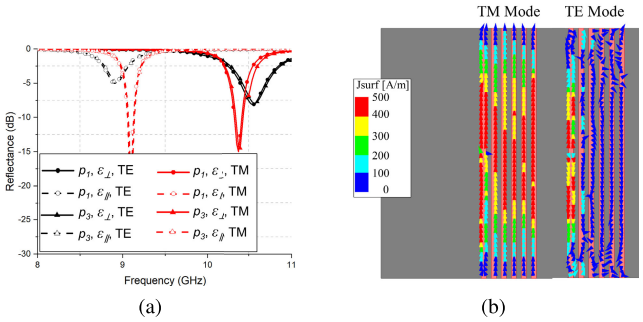

FIGURE 3. (a) Frequency responses versus offset position $p_{\#}$ (solid lines: zero bias state ($\varepsilon_{\perp}$, dashed lines: saturation states ($\varepsilon_{\parallel}$, black: TE mode, red: TM mode, circle symbols: p_1, triangle symbols: p_3), and (b) current distribution on the bias line for the TM mode at the resonance frequency.

LC (Merck KGaA, Darmstadt, Germany) was employed in this work. Based on the datasheet, the tunable range of the dielectric constant of the LC adopted here is expected to be in the range of 2.5–3.5 (from $\varepsilon_{\perp}$ to $\varepsilon_{\parallel}$). The corresponding loss tangent decreases from 0.012 to 0.0064. The periodicity of the cells was set at 10 mm.

Fig. 3 shows the simulation results for the LCRA cell using ANSYS HFSS. The frequency response versus the via position for each polarization is shown in Fig. 4(a). Owing to the symmetric topology, the responses of p_1 and p_3 were the same as those of p_4 and p_6. The black and red lines represent the TE and TM mode responses, respectively. In addition, the extreme phase states associated with the initial bias state ($\varepsilon_{\perp}$) and saturation state ($\varepsilon_{\parallel}$) are represented by solid and dashed lines, respectively. Unlike the responses of the TE waves, extremely large losses occurred in the TM case due to the RF current induced on the bias lines, as shown in Fig. 3(a). Because of the asymmetric geometry, the responses for TE and TM modes differ. Fig. 3(b) shows the RF current distribution at the resonant frequency in the TE and TM modes. The current density of TM waves is higher than that of TE waves because more current is induced by the electric fields parallel to the bias lines, resulting in RF losses. To reduce the effect of the bias line in the TM cases, this study

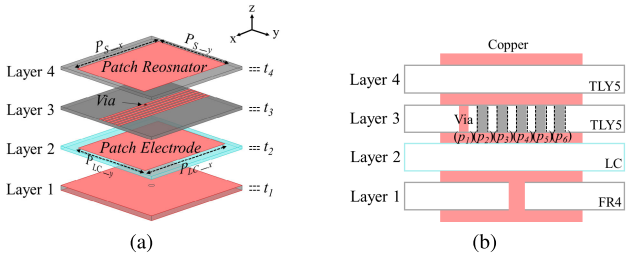

FIGURE 4. (a) Final design and (b) side view of the proposed LCRUC.

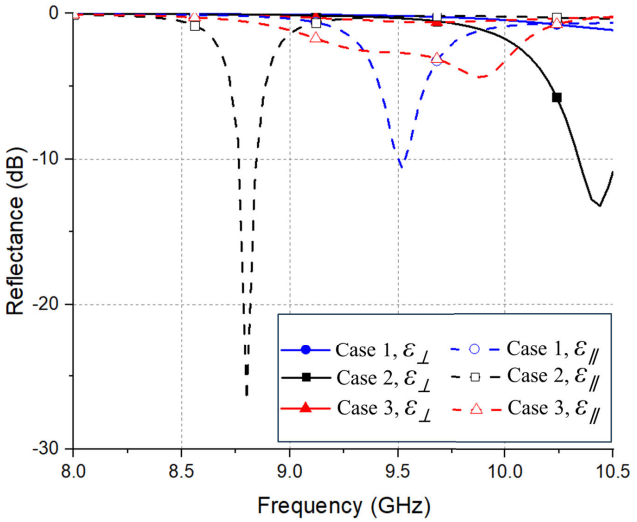

FIGURE 5. Reflection loss responses versus frequency at various patch dimensions (case 1: $Ps\_x = Ps\_y = P_{LC}\_x = P_{LC}\_y = 8.4$ mm, case 2: $Ps\_x = Ps\_y = P_{LC}\_x = 8.4$ mm; $= P_{LC}\_y = 9.0$ mm, and case 3: $Ps\_x = Ps\_y = 9.0$ mm; $= P_{LC}\_x = P_{LC}\_y = 8.4$ mm).

introduces a metal shield with a lateral dimension larger than that of the electrode patch was introduced.

Fig. 4(a) and (b) show the proposed LCRA unit cell (LCRUC) where an additional metal patch was introduced to the top of the unit cell. The role of the metal patch can be interpreted in two ways. One is as an impedance tuner, which is further explained in the Appendix. In terms of an equivalent circuit, the metal patch can be modeled as a capacitance. With the addition of this capacitance, a resonant frequency is generated due to the added capacitance, and by increasing the real term of the impedance, the reflection loss can be significantly reduced. Another interpretation is that the metal patch replaces the existing LC resonator's electrode with the main resonator and acts as a metal shield. Therefore, by covering the bias line, less RF current is induced, which also helps reduce the reflection loss.

It should be noted that the lateral dimension of the shield has to be larger than that of the patch electrode to create the desired resonance. Fig. 5 shows the frequency responses versus lateral patch dimensions for TM polarization. The solid and dashed lines represent the initial bias state ($\varepsilon_\perp$) and saturation state ($\varepsilon_\parallel$), respectively. Three cases were considered, and the loss in case 3 was small. If the lateral dimension of the patch electrode is larger than that of the

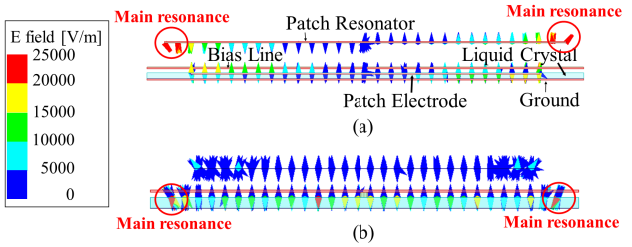

FIGURE 6. Field plot @9.65 GHz versus two cases (a) $P_{LC}\_x, y < Ps\_x, y$, and (b) $P_{LC}\_x, y > Ps\_x, y$ for TM mode.

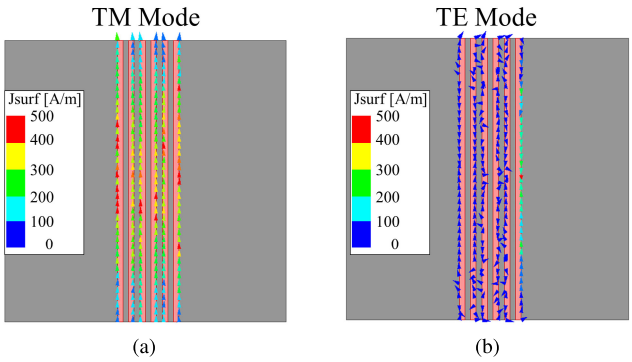

FIGURE 7. Current distribution on the bias line for (a) the TM mode (b) the TE mode at the resonance frequency of the proposed LCRUC.

patch resonator (case 2) for the main resonance in the claimed band, the RF current deteriorates, resulting in an extremely high loss. However, in case 3, there was a low loss owing to the electric field distribution, as shown in Fig. 3(b). The patch resonator serves as a metal shield for the RF current and resonates with the RF ground with less effect from bias lines.

Fig. 6(a) and (b) show the field distribution plots for two different cases—when $P_{LC}\_x, y < Ps\_x, y$ and $P_{LC}\_x, y > Ps\_x, y$, respectively—for TM modes at 9.65 GHz. Depending on the dimensions of the metal patch and the electrode, the main resonance occurs at different layers at 9.65 GHz. When $P_{LC}\_x, y < Ps\_x, y$, the main resonance occurs at the electrode, leading to high losses due to the presence of bias lines. In contrast, when $P_{LC}\_x, y < Ps\_x, y$, the main resonance shifts to the additional metal patch, resulting in lower losses due to the shielding effect. Finally, the dimensions of the metal patch and the electrode are selected so that they resonate at the desired frequency band for both the TE and TM modes.

Fig. 7 shows the current distribution on the bias line for both the TM and TE modes at the resonance frequency of the proposed LCRUC. Although these currents, which degrade RF performance, are more pronounced in the TM mode than in the TE mode, they are significantly reduced compared to those observed in Fig. 3(b), thanks to the metal shielding provided by the additional patch.

Fig. 8 depicts the magnitude responses and phase dynamic range of the final design of the proposed LCRUC versus the

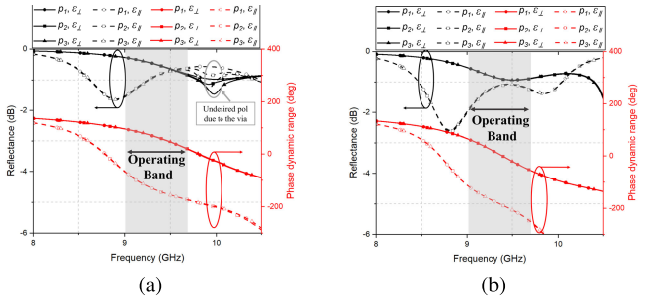

FIGURE 8. Reflectance responses versus frequency in (a) the TE mode responses and (b) the TM responses versus via offset position p# of the proposed LCRUC (solid lines: zero bias state ($\varepsilon_\perp$), dashed lines: saturation state ($\varepsilon_\parallel$), black: magnitude, and red: reflection phase responses.

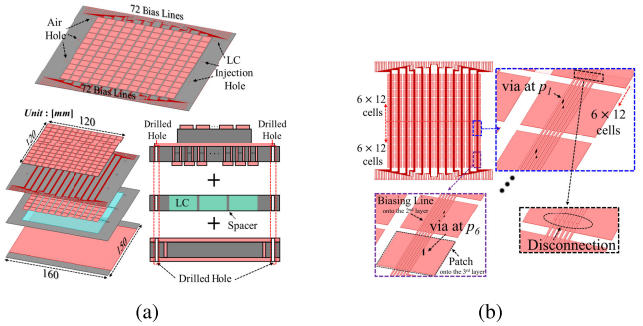

FIGURE 9. (a) Enlarged and side views of the proposed DLP-LCRA and (b) the top view of the bridge-shaped biasing topology and details.

extreme bias states at p_1-p_3 for each polarization. The black and red lines represent the magnitude and phase responses, respectively. The offset position of the metallic via affects the responses in the TE mode, resulting in an undesired resonance that is not in the claimed frequency band. The maximum reflection loss and phase dynamic range are 1.8 dB and 240° in the TE mode, and those are 2.2 dB and 260° in the TM mode, respectively. The operating band exhibits a stable gain variation of 1 dB across the bandwidth. The geometric parameters of the final design are listed in Table 1.

TABLE 1. Geometric parameters of the proposed LCRUC.

Parameter	Ps_x	Ps_y	P_{LC}_x	P_{LC}_y
Value	9 mm	8.6 mm	8.8 mm	8.2 mm
Parameter	t_1	t_2	t_3	t_4
Value	0.4 mm	0.25 mm	0.13 mm	0.51 mm
Parameter	L_w	L_g	P_1	P_2
Value	0.2 mm	0.2 mm	-0.9 mm	-0.5 mm
Parameter	P_3	P_4	P_5	P_6
Value	-0.1 mm	0.1 mm	0.5 mm	0.9 mm

III. DESIGN AND MEASURED RESULTS OF THE DLP-LCRA

A. DESIGN AND FABRICATION PROCESS OF THE DLP-LCRA

The section describes the proposed biasing topology of the DLP-LCRA in detail as well as the fabrication process, including the integration substrates and LC injection. In addition, the measurement setup, reflection phase extraction, and beamforming results are presented to demonstrate the proposed structure.

Fig. 9 illustrates an enlarged view of the proposed DLP-LCRA and the biasing topology. Unlike the other layers, the first layer with dimensions of 120 ×120 mm^2 was filled with the LC, as shown in Fig. 11(a). Other areas under the first layer exist for biasing lines stretched to the edges of the second layer, where 0.2 ϕ holes were drilled and pin headers were embedded. In total, 144 biasing lines were introduced to form the antenna beam. The third layer was divided into three compartments to create a cavity that accommodates the LC. Spacers between the compartments supported the layer. In the fourth layer, metallic vias were introduced for easy integration of the DC ground. The fabrication processes of the proposed DLP-LCRA were as follows: 1) The three parts were fabricated using a PCB process. 2) The three parts were integrated into one. 3) The LC was injected into the three cavities. When the LC was injected into the LC holes, the air slowly escaped. Three pairs of injection and air holes were employed to match the three compartments. The total dimensions of the proposed DLP-LCRA are 150 ×160 mm^2, with bias lines placed on the surface. There are certain trade-offs in the design to achieve dual-polarization responses. For example, embedded vias in the layer 4 substrates increase manufacturing complexity. However, to prevent LC leakage, the use of embedded vias is essential.

Fig. 9(b) illustrates the second layer, which consists of biasing lines and patch electrodes. In the proposed biasing topology, indicated by the black dashed box, the center lines were cut to achieve 2D beamforming. Therefore, two sets of 6–12 biased lines were arranged. In addition, the metallic vias at p_1–p_6 in the blue and purple dashed boxes were connected to the corresponding line to provide various bias-voltage signals to each LC cavity. This topology enables the 2D beamforming and dual-polarization responses.

B. EXPERIMENTAL SETUP AND RESULTS

The section introduces and discusses the proposed DLP-LCRA sample, phase extraction, and measured results. Considering that the intermediate states of the LC are difficult to extract owing to anisotropy and inhomogeneity, the phase-extraction method can be useful for obtaining the desired phase for the applied bias voltage.

Fig. 10 illustrates a photograph of the proposed DLP-LCRA fixed to a support structure. The supporting structure was fabricated using 3D printing technology, and an additional region outside the reconfigurable region of the DLP-LCRA was covered with absorbers to avoid unwanted scattering. A standard horn antenna with a gain of 16.5 dBi at 9.65 GHz was chosen as the feed antenna, and the focal distance between the feed and the LCRA was 12 cm with an offset angle of 20°. The focal length was calculated by obtaining the spillover and taper efficiency [25]. The control

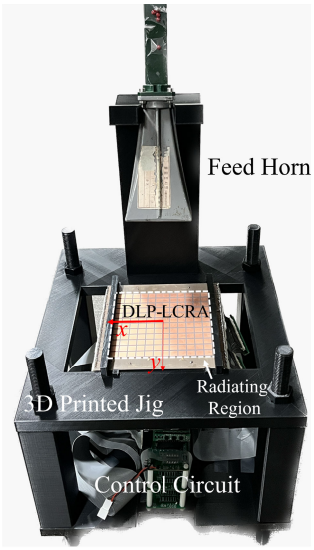

FIGURE 10. Photograph of the fabricated DLP-LCRA supported by 3D printed jig with a control circuit.

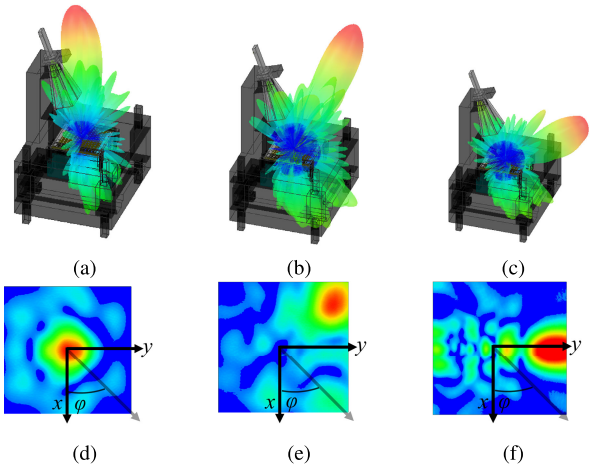

FIGURE 11. (a)-(c) 3D beam pattern restults and (d)-(f) field distribution corresponding to the beam pattern on the xy-planes. ((a), (d) $\theta = \varphi = 0°$, (b), (e) $\theta = 30°$, $\varphi = 45°$, (c), (f) $\theta = 90°$, $\varphi = 60°$.

circuit provided an external voltage from 0 to 30 V in 0.1 V steps within 144 output channels.

Fig. 11 illustrates the 3D beam patterns of the proposed DLP-LCRA at different angles. The results confirm that the proposed structure can steer not only in the E- and H-planes but also along the D-plane. Four arbitrary angles were selected to demonstrate its 2D coverage. Thanks to the biasing topology, each unit cell can be controlled independently. The field distributions corresponding to the beam pattern plots on the xy-planes are shown in Fig. 11(d), (e), (f).

Fig. 12 illustrates the measurement setup to obtain phase-voltage curves and beam patterns for each polarization case. Because of the anisotropy and inhomogeneity of the intermediate states in the LC, the bias voltage for the desired phase shift should be extracted. The measurement tasks

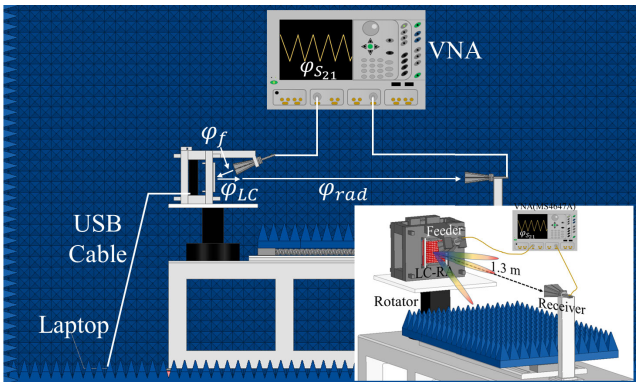

FIGURE 12. Measurement setup for obtaining phase-voltage curves for both polarization cases.

were implemented in an anechoic chamber, and reflection phase extraction was performed using a vector network analyzer (VNA) (MS4647A, Anritsu). The distance between the reflectarray and the receiver is set to 1.3 m. The proposed DLP-LCRA is mounted on a rotator to enable angular scanning. The bias code is provided via the laptop connected through a USB cable, which interfaces with the controller.

The overall measurement procedure is illustrated in Fig. 13. The process begins with a two-port SOLT (Short-Open-Load-Thru) calibration, followed by verification using standard references. The calibration is considered valid if the reflection coefficients (S_{11}, S_{22}) for open/short and load conditions are approximately 0 dB $\pm$ 0.1 dB and below -40 dB, respectively, and the transmission coefficients (S_{21}, S_{12}) are around 0 dB $\pm$ 0.1 dB with phase error less than 5°. Once the calibration is verified, the device under test (DUT) is set up, and the S_{21} phase is measured for both X- and Y-polarizations as a function of the applied bias voltage. This continues until phase saturation is observed. The bias voltage was obtained using the following steps: 1) Apply the same voltage to all cells 2) Check the S21 phase by using the VNA 3) Calculate the phase difference from the phase at the zero bias. The phase difference is expressed by ((1))

$$\varphi_{S_{21}} = \varphi_f + \varphi_{LC} + \varphi_{rad} \tag{1}$$

where φ_f refers to the phase shifts from the feed antenna, φ_{LC} represents the reflection phase shifts as a result of the change in the LC, and φ_{rad} refers to the phase shift of the radiated waves from the reflectarray to the receiver. After calibration, beam pattern measurements are performed based on the reference phase configuration. The gain is evaluated, and if it does not reach its maximum, the bias setting is adjusted, and the measurement loop is repeated. Once the maximum gain is achieved, additional beam patterns are measured at various scanning angles. Finally, 3 dB coverage is established to evaluate the beam-steering capability of the proposed structure. The extracted reflection phase responses for the two polarization responses as functions of the bias voltage are presented in Fig. 14. The phase difference between 0 V

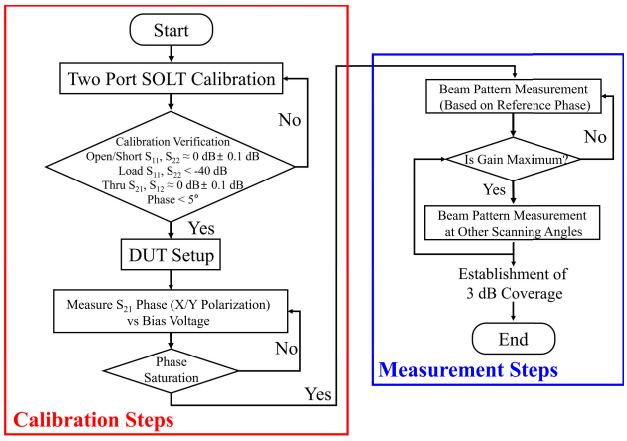

FIGURE 13. Measured results of phase-voltage curves.

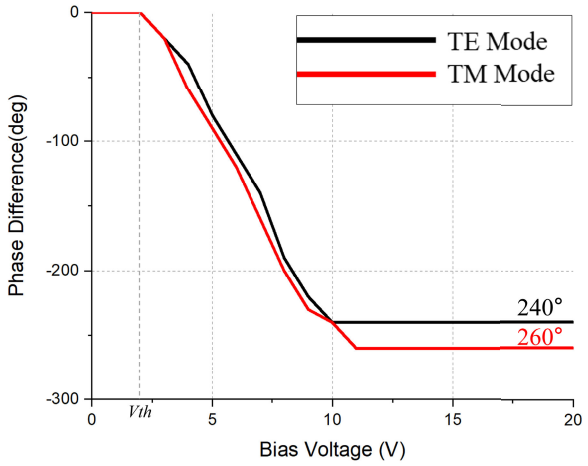

FIGURE 14. Measured results of phase-voltage curves.

and a certain bias state is depicted, and the maximum phase difference matches the dynamic phase range of the unit cell obtained using the full-wave simulator.

Fig. 15(a) and (b) show the measured H- and E-plane beam patterns for the TE cases at 9.65 GHz. On the H-plane, that is, the measured gain and SLL are in the ranges of 16.7–18.5 dBi and −16.50—10.02 dB, respectively. Beam coverage was confirmed from −49° to +51°. In addition, on the E-plane, the measured gain and SLL are in the ranges of 16.5–19.4 dBi and −11.07—5.66 dB, respectively. The beam coverage ranges from 0° to 62°. The waves reflected toward the feed antenna were degraded because of the blockage.

Fig. 16(a) and (b) show the measured results of the E- and H-plane beam patterns, respectively, for the TM cases at 9.65 GHz. On the E-plane, the measured gain and SLL are in the ranges of 15.8–18.1 dBi and −11.31—8.61 dB, respectively. Beam coverage was confirmed from −50° to +50°. On the H-plane, the measured gain and SLL are in the ranges of 16.8–18.5 dBi and −15.28—7.45 dB, respectively. The beam coverage ranges from 0° to 60°. The beam coverage was based on a 3 dB gain variation.

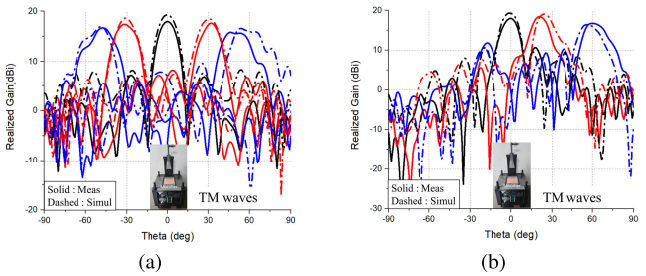

FIGURE 15. Simulated and measured beam patterns for TE waves (a) on the xoz and (b) yoz planes.

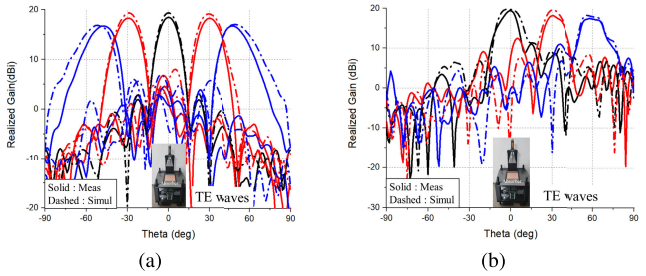

FIGURE 16. Simulated and measured beam patterns for TM waves (a) on the xoz and (b) yoz planes.

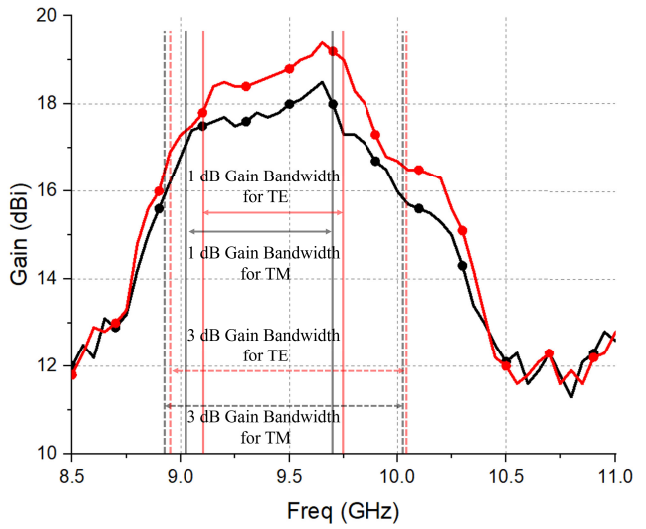

FIGURE 17. Measured gains versus operating frequency range (red line: TE mode, black line: TM mode).

Fig. 17 illustrates the measured gains versus the operating frequency range. The 1-dB gain bandwidths of the TE and TM modes (illustrated by solid lines) are in the ranges of 9.15–9.75 GHz and 9.05–9.7 GHz, respectively. The 3-dB gain bandwidths of the TE and TM modes (illustrated by dashed lines) are in the ranges of 8.9–10.2 GHz and 9–9.95 GHz, respectively.

Table 2 presents a comparison of the performance of all LCRAs from the microwave band to the terahertz band. It appears that many LCRAs are capable of steering the beam in 2D, and the LCRA in [13] has limited scanning

TABLE 2. Performance comparisons of LCRA Antennas.

	Frequency [GHz]	Aperture Efficiency [%]		Side Lobe Level (SLL) [dB]		Coverage	Scanning Range [°]				Dimension [λ_0^2]	Polarization	Fabrication
[18]	24	5.8		-		1D	-60-0				15 × 7.2	Single	Glass
[17]	24	23.1		-		2D	E-Plane		H-Plane		6 × 6	Single	PCB
							-45-45		-45-45				
[22]	28	15		-		2D	E-Plane		H-Plane		4.2 × 4.2	Dual	Glass
							-15-55		-50-50				
[19]	9.55	35.8		-15.5		2D	E-Plane		H-Plane		3.82 × 3.82	Single	PCB
							0-65		-50-50				
[27]	35.5	38.9		-15.3		2D	E-Plane		H-Plane		4.97 × 4.97	Single	Glass
							0-60		-50-50				
[28]	28.5	25.3		-		2D	E-Plane		H-Plane		3.74 × 3.74	Dual	Glass
							-45-45		-45-45				
[23]	98	24		-9		1D	5-40				-	Dual	Glass
[26]	-	22.5		-		2D	E-Plane		H-Plane		3.74 × 3.74	Dual	Glass
							-50-50		-20-50				
[13]	37.5	-		-		2D	E-Plane		H-Plane		5 × 4.875	Single	Glass
							-30-30		0-42				
This Study	9.65	TE	TM	TE	TM	2D	TE		TM		3.86 × 3.86	Dual	PCB
		46.5	37.8	-16.5	-15.3		E-Plane	H-Plane	E-Plane	H-Plane			
							0-62	-49-51	-50-50	0-60			

TABLE 3. Efficiency budgets of the proposed DLP-LCRA for each polarization.

Efficiencies [%]	TE	TM
Reflection	0.931	0.872
Phase	0.901	0.925
Taper	0.872	0.872
Spillover	0.881	0.881
Edge	0.938	0.938
Polarization	0.995	0.989
Blockage	0.794	0.794
etc.	0.974	0.828
Total	0.465	0.378

capabilities that can only steer the beam in the E- or H-planes. Additionally, the proposed structure achieves a maximum aperture efficiency of 46.5 %, representing a 106.67 % increase compared to [23]. The proposed bridge-shaped biasing topology enables the simultaneous realization of dual polarization and 2D beam steering, while the additional patch contributes to achieving high aperture efficiency. Table 3 lists the efficiency budget for each polarization used to explain the high aperture efficiencies. The aperture efficiency of the reflectarray can be divided as expressed in ((2)),

$$\varepsilon_{aperture} = \varepsilon_{reflection} * \varepsilon_{phase} * \varepsilon_{spillover} * \varepsilon_{edge} * \varepsilon_{polarization} * \varepsilon_{blockage} * \varepsilon_{etc} \quad (2)$$

where reflection is the average reflected energy from the unit cells, and the phase efficiency represents the phase dynamic range and quantization losses. The taper, spillover, and edge efficiencies are related to the feed antenna and configuration of the reflectarray aperture. The power received at the aperture and the uniformity of the power amplitude indicate the spillover and taper efficiency, respectively. The edge-taper loss increased when the incident waves that diffracted from the edge of the aperture increased. The polarization efficiency can be calculated as the ratio of co-polarized waves to the sum of co- and cross-polarized waves. Blockage loss occurs when the scattered waves from the reflectarray are blocked by a feed antenna. The fabrication and coupling losses were classified as efficiencies.

IV. CONCLUSION

This study proposed PCB process-based DLP-LCRA with high aperture efficiency, 2D coverage, and low SLL. By introducing bridge-shaped biasing topology, the proposed DLP-LCRA can achieve 2D coverage. In addition, due to the limitation of the resolution of PCB process, RF current should be carefully treated to reduce RF losses for dual-polarization responses. The deleterious effect of the biasing layer on the TM modes was reduced by adding a metallic patch and increasing the dielectric thickness. Additionally, a bridge-shaped biasing topology was introduced in which the uniformly arranged biasing layer did not affect the TM mode responses according to the number of biasing lines. By using a metallic via, the proposed biasing layer enables the formation of a 2D beam. The effects of the biasing layer on the two polarization responses were verified using full-wave and circuit simulations. Accordingly, an aperture efficiency of 46.5 % and an SSL value of −16.5 dB were attained. The proposed DLP-LCRA is promising for designing dual-polarization LCRAs with high efficiency, broad beam coverage, and 2D beam-scanning. The proposed DLP-LCRA will be a promising solution for dual-polarization LCRA fabricated by PCB-process. To extend the design to higher operating frequencies, the DLP-LCRA can be realized by scaling down the aperture proportionally to the frequency. In addition, operating at higher frequencies enables cost reduction in large-scale production of the DLP-LCRA, as the aperture size and the amount of LC required decrease. This study paves the way for intelligent surface or real-time electronically reconfigurable antennas for future 6G communication systems.

APPENDIX

This section describes the equivalent circuit of the proposed LCRUC for each polarization.

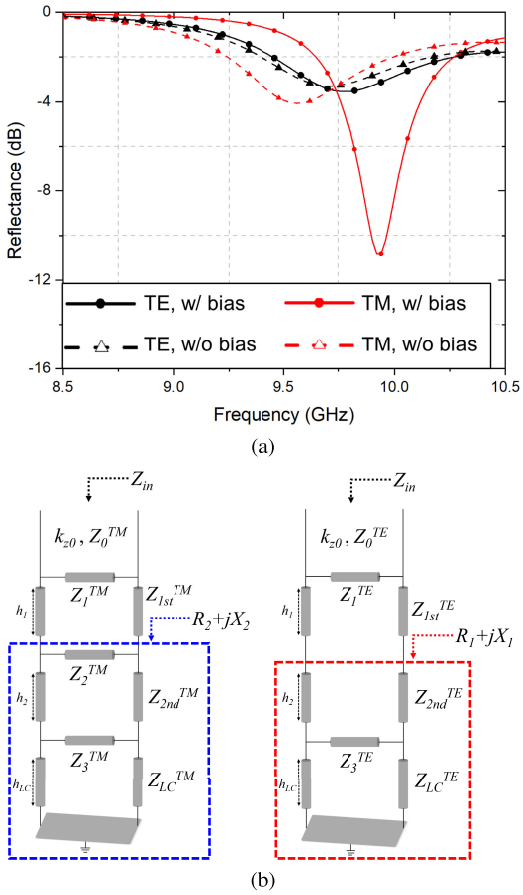

FIGURE 18. (a) Reflection coefficient versus frequency responses in the with (w/) and without (w/o) biasing layer cases (solid lines: w/ biasing lines, dashed lines: w/o biasing lines, black: TE mode, and red: TM mode) and (b) the corresponding equivalent circuits.

Fig. 18(a) illustrates the magnitude responses for each polarization w/ and w/o bias layers. To construct equivalent circuits, the metallic via between the biasing line and the metallic patch on the third layer was not considered in the simulation results. The via effect is illustrated in Fig. 5(a). Assuming lossless to layers 1 and 2 and no interlayer coupling effect, the corresponding equivalent circuits for each polarization are presented in Fig. 4. The left- and right-side networks depict the equivalent circuits for the TM and TE modes in an infinite periodic array of the DLP-LCRUC. The propagation constant k_0 represents a semi-infinite free space. The TE and TM mode characteristic impedances are $Z_0^{TE} = \omega\mu_0/k$ and $Z_0^{TM} = k/\omega\epsilon_0$, respectively, where $Z_c^{TM} = k/\omega\epsilon_0$ and $Z_c^{TE} = \omega\mu_0/k$ are the characteristic impedances of the TE and TM modes. The propagation constant is k is defined as $k = \sqrt{(k_0^2 - k_t^2)}$, where $k_t = k_0 sin\theta$ is the transverse wavenumber. When the normal angle of incidence is considered, the value of $\theta = 0°$, and the TM and TE waves become x- and y-polarized waves, respectively.

For the TE and TM modes, the shunt impedances related to the metallic patch array were modeled as $Z_1^{TM(TE)} = j\omega L_1^{TM(TE)} - j/\omega C_1^{TM(TE)}$ [27].

$$C_1^{TM} = \varepsilon_0\varepsilon_{eff\,1}\frac{2D}{\pi}log(csc\frac{\pi D - Ps\_x(y))}{2D}) \tag{3}$$

$$C_1^{TE} = \varepsilon_0\varepsilon_{eff\,1}\frac{2D}{\pi}log(csc\frac{\pi D - Ps\_x(y))}{2D})(1 - \frac{k_0^2}{k_{eff\,1}^2}\frac{sin^2\theta}{2}) \tag{4}$$

$k_{eff\,1} = k_0\sqrt{\varepsilon_{eff\,1}}$ is the effective propagation constant in an effective host medium with an effective permittivity $\varepsilon_{eff\,1}$ [28]. The inductance Z_1 can be effectively calculated using a full-wave simulator [29]. The LC employed here is a lossy material that imposes the metallic patch, and the ground slab of the LC layer is modeled as $Z_3^{TM(TE)} = R_3 + j\omega L_3^{TM(TE)} - j(1/\omega C_3^{TM(TE)})$ and $Z_{LC}^{TM(TE)} = R_3 + j\omega L_{LC}$.

$$C_3^{TM} = \varepsilon_0\varepsilon_{eff\,2}\frac{2D}{\pi}log(csc\frac{\pi D - P_{LC\_x(y)})}{2D}) \tag{5}$$

$$C_1^{TE} = \varepsilon_0\varepsilon_{eff\,2}\frac{2D}{\pi}log(csc\frac{\pi D - P_{LC\_x(y)})}{2D}) \times (1 - \frac{k_0^2}{k_{eff\,2}^2}\frac{sin^2\theta}{2}) \tag{6}$$

Because the metallic patches introduced in this study were printed on a thin dielectric substrate, higher-order Floquet mode reflections from the ground plane should be considered [30].

$$C_{mod}^{TM(TE)} = C_3^{TM(TE)} - \frac{2D\varepsilon_0\varepsilon_{eff\,2}}{\pi}log(1 - e^{\frac{-4\pi t_{LC}}{D}}) \tag{7}$$

The resistance of the metallic patches adjacent to the LC layer is expressed as

$$R_3 = \frac{-\varepsilon''_{LC}}{\omega\varepsilon_{eff\,2}C_3^{TM(TE)}} \tag{8}$$

$$R_{LC} = \frac{k_2}{\omega\varepsilon_0\varepsilon'_{LC}}[\frac{-\varepsilon''_{LC}}{\varepsilon'_{LC}}tan(k_2t_3) - t_3\frac{k_2\varepsilon''_{LC}}{2\varepsilon'_{LC}}(1 + tan^2(k_2t_3)] \tag{9}$$

$$L_{LC} = \frac{k_2}{\omega\varepsilon_0\varepsilon'_{LC}}tan(k_2t_3) \tag{10}$$

A grounded dielectric slab with thickness t3 is expressed according to 10. $k_2 = k_0\sqrt{\varepsilon_{eff\,2}}$ represents the propagation constant of the LC. The lossless transmission lines related to $Z_{1st(2nd)}^{TM(TE)}$ are $j\omega L_{1(2)} = j\omega\mu_0 t_{1(2)}$ of the series inductor, where the μ_0 means free space permeability. Z_2^{TM} denotes the bias in the second layer. Although the metal strip line is expressed in [18], the impedance of the biasing layer should be carefully chosen because of the coupling between the biasing lines. The value of Z_2^{TM} can be calculated using a full-wave simulator using [29] or a circuit simulator.

Fig. 19(a) depicts the two-port Floquet simulation setup in the full-wave simulator used to calculate Z_2^{TM}. As shown in the corresponding equivalent circuit, the capacitance

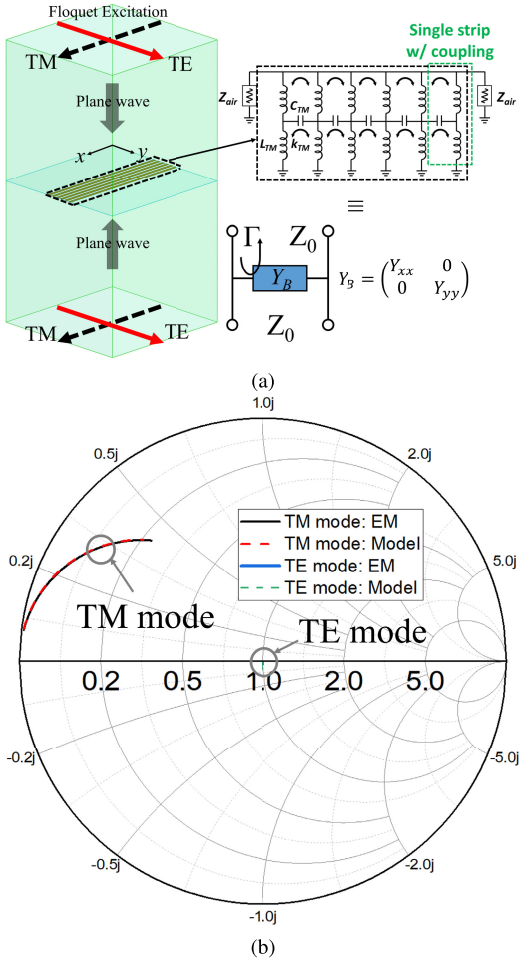

FIGURE 19. Floquet simulation setup of the biasing layer with the corresponding equivalent circuit and (b) frequency responses of the reflection coefficient of the two modes.

and mutual inductance between the adjacent lines were considered. Fig. 19(b) illustrates the full-wave and circuit simulation results. Considering the periodicity of the unit cell, the simulated frequency range was set to 2–15 GHz to avoid grating lobes [31].

$$Y_B = \frac{-Z_0(1+\Gamma)}{2\Gamma} \tag{11}$$

As shown in Fig. 19(a), Y_B is modeled differently with respect to the mode, where Y_{xx} (TM mode) is seen as inductive in the claimed frequency band, and Y_{yy} (TE mode) is matched. The parameters in the red box are general models of the conventional LCRUC. The input impedances of the TM and TE modes equivalent circuits are expressed by 12 and 13, respectively.

$$Re\{Z_{in}\} = \frac{R_2}{(\omega C_1^{TM} R_2)^2 + (\omega^2 C_1^{TM} L_1 + \omega C_1^{TM} X_2 - 1)^2} \tag{12}$$

$$Re\{Z_{in}\} = \frac{R_1}{(\omega C_1^{TE} R_1)^2 + (\omega^2 C_1^{TE}(L_1+L_2) + \omega C_1^{TE} X_1 - 1)^2} \tag{13}$$

In addition, the maximum reflection loss occurs at resonance, as defined in 14. Thus, if the real input impedance of the unit cell increases, the reflection loss can be reduced.

$$\Gamma \simeq \frac{Re\{Z_{in}\} - Z_0}{Re\{Z_{in}\} + Z_0} \tag{14}$$

In contrast to the conventional design modeled as the red box in Fig. 18(b), the proposed design reduces the reflection loss without increasing the LC thickness. This is accomplished by placing a metallic patch in the first layer.

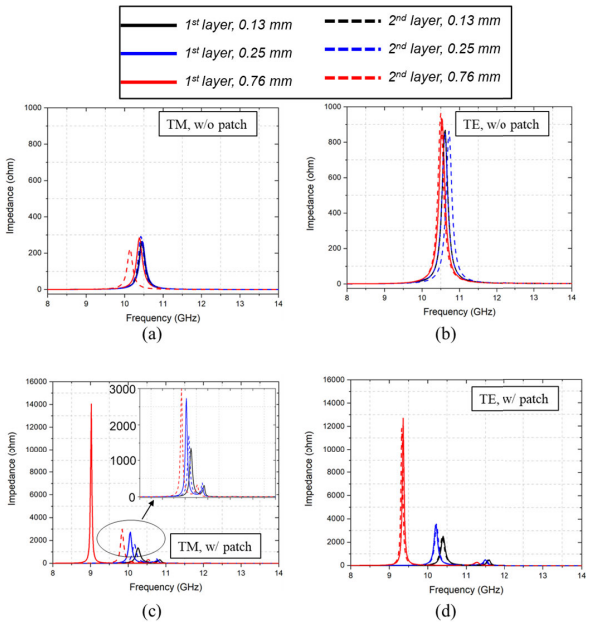

FIGURE 20. Real impedances of the TM and the TE modes responses w/ and w/o the metallic patch onto the first layer. (a) TM, w/o patch; (b) TE, w/o patch; (c) TM, w/ patch; and (d) TE, w/ patch).

Fig. 20 illustrates the real impedance results related to the parametric studies of the first- and second-layer thicknesses. The results were obtained by assuming a normal angle of incidence to extract the TE and TM mode responses. Fig. 20(a) depicts the real impedance in the blue box in Fig. 18(b) added by an inductance modeled by the first substrate ($R_2 + jX_2 + j\omega L_1$). Additionally, Fig. 20(a) represents real impedance results in the red box in Fig. 18(b) added by an inductance modeled by the second substrate ($R_1 + jX_1 + j\omega L_2$). In the absence of a metallic patch, the real impedance does not increase as the thickness of the first or second layer increases, as shown in Fig. 20(a) and (b). However, if a metallic patch is present, the real impedance increases with the thickness of the first or second layer, as shown in Fig. 20(c) and (d), respectively. Consequently, the metallic patch affects the reflection loss. In particular, the TM-mode responses that are deteriorated by the biasing layer can be improved, eventually leading to a dual-polarized reflectarray.

A metallic patch can also be used to miniaturize the unit cell dimensions by increasing the substrate thickness, as shown in Fig. 20(c) and (d).

REFERENCES

[1] M. R. Chaharmir and J. Shaker, "Design of a multilayer X-/Ka-band frequency-selective surface-backed reflectarray for satellite applications," *IEEE Trans. Antennas Propag.*, vol. 63, no. 4, pp. 1255–1262, Apr. 2015.

[2] D. R. Prado, M. Arrebola, M. R. Pino, and G. Goussetis, "Multi-frequency broadband optimization of spaceborne reflectarrays for space applications," in *Proc. Int. Workshop Antenna Technol. (iWAT)*, Feb. 2020, pp. 1–4.

[3] H. Yang, S. Kim, H. Kim, S. Bang, Y. Kim, S. Kim, K. Park, D. Kwon, and J. Oh, "Beyond limitations of 5G with RIS: Field trial in a commercial network, recent advances, and future directions," *IEEE Commun. Mag.*, vol. 62, no. 10, pp. 132–138, Oct. 2024.

[4] Z. Xu, J. Ding, G. Chen, G. Zhao, and Y. Zhang, "An approach to high frame rate radar imaging through electronically displaced-phase-center antenna," *IEEE Trans. Geosci. Remote Sens.*, vol. 58, no. 8, pp. 5602–5611, Aug. 2020.

[5] H.-G. Kim, J.-Y. Kim, and J.-S. Oh, "Design and implementation of an X-band liquid-crystal-based active reflectarray antenna," *J. Korean Inst. Electromagn. Eng. Sci.*, vol. 32, no. 10, pp. 878–887, Oct. 2021.

[6] S. Costanzo, F. Venneri, A. Raffo, and G. Di Massa, "Dual-layer single-varactor driven reflectarray cell for broad-band beam-steering and frequency tunable applications," *IEEE Access*, vol. 6, pp. 71793–71800, 2018.

[7] H. Legay, B. Pinte, M. Charrier, A. Ziaei, E. Girard, and R. Gillard, "A steerable reflectarray antenna with MEMS controls," in *Proc. IEEE Int. Symp. Phased Array Syst. Technol.*, Oct. 2003, pp. 494–499.

[8] X. Meng, M. Nekovee, and D. Wu, "The design and analysis of electronically reconfigurable liquid crystal-based reflectarray metasurface for 6G beamforming, beamsteering, and beamsplitting," *IEEE Access*, vol. 9, pp. 155564–155575, 2021.

[9] A. R. Ndjiongue, T. M. N. Ngatched, O. A. Dobre, and H. Haas, "Re-configurable intelligent surface-based VLC receivers using tunable liquid-crystals: The concept," *J. Lightw. Technol.*, vol. 39, no. 10, pp. 3193–3200, May 15, 2021.

[10] G. Perez-Palomino, J. Encinar, R. Dickie, and R. Cahill, "Preliminary design of a liquid crystal-based reflectarray antenna for beam-scanning in THz," in *Proc. IEEE Antennas Propag. Soc. Int. Symp. (APSURSI)*, Jul. 2013, pp. 2277–2278.

[11] H. Kim, S. Oh, S. Bang, H. Yang, B. Kim, and J. Oh, "Independently polarization manipulable liquid-crystal -based reflective metasurface for 5G reflectarray and reconfigurable intelligent surface," *IEEE Trans. Antennas Propag.*, vol. 71, no. 8, pp. 6606–6616, Aug. 2023.

[12] H. Kim, J.-W. Lee, J. Wang, M.-S. Kim, H.-R. Kim, and J. Oh, "Waveguide-thru closed-form characterization of anisotropic polymer network liquid-crystal for mmWave reconfigurable RF devices," *IEEE Trans. Antennas Propag.*, vol. 72, no. 7, pp. 5447–5457, Jul. 2024.

[13] X. Li, H. Sato, H. Fujikake, and Q. Chen, "Development of two-dimensional steerable reflectarray with liquid crystal for reconfigurable intelligent surface applications," *IEEE Trans. Antennas Propag.*, vol. 72, no. 3, pp. 2108–2123, Mar. 2024.

[14] P. Aghabeyki, P. de la Rosa, M. Caño-García, X. Quintana, R. Guirado, and S. Zhang, "Optically transparent beam-steering reflectarray antennas based on a liquid crystal for millimeter-wave applications," *IEEE Trans. Antennas Propag.*, vol. 72, no. 1, pp. 614–627, Jan. 2024.

[15] K. Lim, J. D. Margerum, A. M. Lackner, L. J. Miller, E. Sherman, and W. H. Smith Jr., "Liquid crystal birefringence for millimeter wave radar," *Liquid Cryst.*, vol. 14, no. 2, pp. 327–337, Jan. 1993.

[16] G. Perez-Palomino, P. Baine, R. Dickie, M. Bain, J. A. Encinar, R. Cahill, M. Barba, and G. Toso, "Design and experimental validation of liquid crystal-based reconfigurable reflectarray elements with improved bandwidth in F-Band," *IEEE Trans. Antennas Propag.*, vol. 61, no. 4, pp. 1704–1713, Apr. 2013.

[17] X. Li, Y. Wan, J. Liu, D. Jiang, T. Bai, K. Zhu, J. Zhuang, and W.-Q. Wang, "Broadband electronically scanned reflectarray antenna with liquid crystals," *IEEE Antennas Wireless Propag. Lett.*, vol. 20, pp. 396–400, 2021.

[18] W. Zhang, Y. Li, and Z. Zhang, "A reconfigurable reflectarray antenna with an 8 μm-thick layer of liquid crystal," *IEEE Trans. Antennas Propag.*, vol. 70, no. 4, pp. 2770–2778, Apr. 2022.

[19] H. Kim, J. Kim, and J. Oh, "Communication a novel systematic design of high-aperture-efficiency 2D beam-scanning liquid-crystal embedded reflectarray antenna for 6G FR3 and radar applications," *IEEE Trans. Antennas Propag.*, vol. 70, no. 11, pp. 11194–11198, Nov. 2022.

[20] H. Kim, J. Kim, and J. Oh, "Liquid-crystal-based X-band reactively loaded reflectarray unit cell to reduce reflection loss," *IEEE Antennas Wireless Propag. Lett.*, vol. 20, pp. 1898–1902, 2021.

[21] P. Aghabeyki, Y. Cai, G. Deng, Z.-H. Tan, and S. Zhang, "A dual-polarized reconfigurable reflectarray with a thin liquid crystal layer and 2-D beam scanning," *IEEE Trans. Antennas Propag.*, vol. 71, no. 4, pp. 3282–3293, Apr. 2023.

[22] P. Aghabeyki, Y. Cai, G. Deng, G. Frølund Pedersen, and S. Zhang, "Beam-scanning reflectarray with switchable polarization based on liquid crystal at millimeter wave," *IEEE Trans. Antennas Propag.*, vol. 73, no. 3, pp. 1894–1899, Mar. 2025.

[23] R. Guirado, G. Perez-Palomino, P. De La Rosa, E. Carrasco, and X. Quintana, "Electronically reconfigurable reflectarray antenna based on single-layer liquid crystal with independent dual-polarization control," *IEEE Trans. Antennas Propag.*, vol. 72, no. 7, pp. 5626–5636, Jul. 2024.

[24] R. Neuder, Y. Liu, N. Dzieia, D. Wang, and A. Jiménez-Sáez, "Unit cell design for dual-polarized liquid crystal reconfigurable intelligent surface based on defected delay lines," in *Proc. 54th Eur. Microw. Conf. (EuMC)*, Sep. 2024, pp. 228–231.

[25] P. Nayeri, F. Yang, and A. Z. Elsherbeni, *Reflectarray Antennas: Theory, Designs, and Applications*. Wiley, 2018, doi: 10.1002/9781118846728.

[26] H. Kim, J.-W. Lee, S. Bang, J. Wang, M.-S. Kim, H.-R. Kim, and J. Oh, "Low-voltage controlled fast switchable liquid-crystal-based reflectarray with transverse rubbing layer," *IEEE Antennas Wireless Propag. Lett.*, vol. 23, pp. 4194–4197, 2024.

[27] O. Luukkonen, C. Simovski, G. Granet, G. Goussetis, D. Lioubtchenko, A. V. Raisanen, and S. A. Tretyakov, "Simple and accurate analytical model of planar grids and high-impedance surfaces comprising metal strips or patches," *IEEE Trans. Antennas Propag.*, vol. 56, no. 6, pp. 1624–1632, Jun. 2008.

[28] F. Costa, "A simple effective permittivity model for metasurfaces within multilayer stratified media," *IEEE Trans. Antennas Propag.*, vol. 69, no. 8, pp. 5148–5153, Aug. 2021.

[29] F. Costa, A. Monorchio, and G. Manara, "Efficient analysis of frequency-selective surfaces by a simple equivalent-circuit model," *IEEE Antennas Propag. Mag.*, vol. 54, no. 4, pp. 35–48, Aug. 2012.

[30] S. A. Tretyakov and C. R. Simovski, "Dynamic model of artificial reactive impedance surfaces," *J. Electromagn. Waves Appl.*, vol. 17, no. 1, pp. 131–145, Jan. 2003.

[31] B. A. Munk, *Frequency Selective Surfaces: Theory and Design*. Hoboken, NJ, USA: Wiley, 2005.

HOGYEOM KIM (Member, IEEE) received the B.S. degree in electrical engineering from Inha University, South Korea, in 2016. He is currently pursuing the integrated M.S. and Ph.D. degree with Seoul National University, South Korea. He was with Korean Army, from 2016 to 2018. His current research interests include transmit/reflectarray antennas, reconfigurable intelligence surfaces for B5G/6G communication, millimeter-wave radar systems, and liquid-crystal material-based metasurfaces.

BYEONGJU MOON (Student Member, IEEE) received the B.S. degree from Sungkyunkwan University, South Korea, in 2021. He is currently pursuing the integrated M.S. and Ph.D. degree with the Department of Electrical and Computer Engineering, Seoul National University, South Korea. His current research interests include metasurfaces, reconfigurable intelligent surfaces for B5G/6G communication, millimeter-wave radar systems, and integrated sensing and communication antenna.

SEUNGWOO BANG (Graduate Student Member, IEEE) received the B.S. degree from Seoul National University of Science and Technology, South Korea, in 2022. He is currently pursuing the integrated M.S. and Ph.D. degree with the Department of Electrical and Computer Engineering, Seoul National University, South Korea. His current research interests include metasurfaces and antenna design.

SEONGWOOG OH (Member, IEEE) received the B.S. degree in electrical engineering and computer science from Gwangju Institute of Science and Technology College, Gwangju, South Korea, in 2016, and the M.S. and Ph.D. degrees in electrical engineering from Seoul National University, Seoul, South Korea, in 2018 and 2023, respectively. From 2023 to 2024, he was a Postdoctoral Researcher with the TICS Research Group, Department of Electrical and Computer Engineering, University of California San Diego. He is currently an Assistant Professor with the Department of Electronics Convergence Engineering, Kwangwoon University, Seoul. His research interests include the design of RF/millimeter-wave integrated circuits, antenna-on-package systems for 5G/6G communication, and microwave brain stimulation. He was a recipient of the 2019 IEEE MTT Seoul Chapter Best Paper Award, the 2022 IEEE AP-S Student Paper Competition Honorable Mention, and the 2022 IEEE Antennas and Propagation Society Fellowship.

JUNGSUEK OH (Senior Member, IEEE) received the B.S. and M.S. degrees from Seoul National University, South Korea, in 2002 and 2007, respectively, and the Ph.D. degree from the University of Michigan, Ann Arbor, MI, USA, in 2012. From 2007 to 2008, he was a Hardware Research Engineer with Korea Telecom and was involved with the development of flexible RF devices. In 2012, he was a Postdoctoral Research Fellow with the Radiation Laboratory, University of Michigan. From 2013 to 2014, he was a Staff RF Engineer with Samsung Research America, Dallas, TX, USA, where he was the Project Leader for a 5G/millimeter-wave antenna systems. From 2015 to 2018, he was a Faculty Member with the Department of Electronic Engineering, Inha University, South Korea. He is currently an Assistant Professor with the School of Electrical and Computer Engineering, Seoul National University. He has published more than 40 technical journal and conference papers. His research interests include mmWave beam focusing/shaping techniques, antenna miniaturization for integrated systems, and radio propagation modeling for indoor scenarios. He was as a TPC Member. He was a recipient of the 2011 Rackham Predoctoral Fellowship Award at the University of Michigan. He served as the Session Chair for IEEE AP-S/USNC-URSI and ISAP. He has served as a Technical Reviewer for (among other journals) IEEE Transactions on Antennas and Propagation and IEEE Antenna and Wireless Propagation Letters.